



http://pubs.acs.org/journal/acsodf Article

# Localized Strain Measurement in Molecular Beam Epitaxially Grown Chalcogenide Thin Films by Micro-Raman Spectroscopy

Qiu Li,\* Yong Wang, Tiantian Li, Wei Li, Feifan Wang, Anderson Janotti, Stephanie Law, and Tingyi Gu\*



Cite This: ACS Omega 2020, 5, 8090-8096



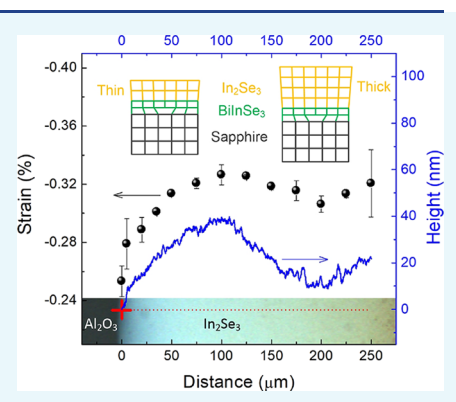
**ACCESS** 

Metrics & More

Article Recommendations

Supporting Information

ABSTRACT: We developed an experimental metrology for measuring local strain in molecular beam epitaxially (MBE) grown crystalline chalcogenide thin films through micro-Raman spectroscopy. For In<sub>2</sub>Se<sub>3</sub> and Bi<sub>2</sub>Se<sub>3</sub> on c-plane sapphire substrates, the transverse-optical vibrational mode (A<sub>1</sub> phonon) is most sensitive to strain. We first calibrated the phonon frequency—strain relationship in each material by introducing strain in flexible substrates. The Raman shift—strain coefficient is -1.97 cm<sup>-1</sup>/% for the In<sub>2</sub>Se<sub>3</sub> A<sub>1</sub>(LO + TO) mode and -1.68 cm<sup>-1</sup>/% for the Bi<sub>2</sub>Se<sub>3</sub> A<sub>1</sub><sup>2</sup>g mode. In<sub>2</sub>Se<sub>3</sub> and Bi<sub>2</sub>Se<sub>3</sub> samples exhibit compressive strain and tensile strain, respectively. The observations are compliant with predictions from the opposite relative thermal expansion coefficient between the sample and the substrate. We also map strain cartography near the edge of as-grown MBE samples. In In<sub>2</sub>Se<sub>3</sub>, the strain accumulates with increasing film thickness, while a low strain is observed in thicker Bi<sub>2</sub>Se<sub>3</sub> films.



## 1. INTRODUCTION

Chalcogenides are a group of two-dimensional (2D) layered materials possessing many interesting optoelectronic properties. Within this large family, topological insulators<sup>1,2</sup> and phase change materials<sup>3-8</sup> receive most of the attention. Their unique properties are applicable to novel on-chip electronic, optoelectronic, and optomechanical devices, such as spinpolarized directional photodetectors, 9,10 broadband photodetectors, 11 and electronic and mechanical memories. 3-7 Those unique electronic and photonic properties of 2D layered materials, such as strong spin-orbit coupling and stoichiometric intercrystalline transitions, are strongly dependent on their atomic arrangements and interlayer interactions, which can be easily deformed during the material preparation processes. Thus, understanding how atomic deformations (e.g. strain and defects) are introduced into atomic structures during the synthesis, exfoliation, and transfer processes is critical to the device efficiency. X-ray and electron diffraction are commonly used to measure the strain in crystalline thin film samples. However, their large spot size limits their applications in device level studies and fail to resolve strain nonuniformity in wafer-scale samples.

Distinguished from bulk separation and other deposition methods, the molecular beam epitaxy (MBE) growth technique can produce large domain single crystalline 2D layered chalcogenide thin films. <sup>5,13–15</sup> The weak interlayer van der Waals (vdW) force allows easy exfoliation of single domain crystalline layers and the formation of dangling bond-free interfaces of the layered material, but it also poses challenges for the choice of the lattice-matched substrate. With the

assistance of wetting layers, high-quality crystalline  $\mathrm{Bi}_2\mathrm{Se}_3$  and  $\mathrm{In}_2\mathrm{Se}_3$  thin films can grow epitaxially on sapphire substrates. S,14 Both materials have a layered structure, which belongs to the space group  $D_{3\mathrm{d}}^5(R\overline{3}m)$ . The unit cell is composed of five atomic layers, that is, 1 quintuple layer (QL):  $\mathrm{SeII-In}(\mathrm{Bi})-\mathrm{SeI-In}(\mathrm{Bi})-\mathrm{SeII}$ . Even with slight lattice constant offsets, strain can still be developed on the interfaces during the epitaxial growth. The accumulation of strain alters the electronic structure and leads to undesired defects, such as threading dislocations and cracking. This work will be dedicated to studying the strain/stress development with the thickness of the epitaxial layer, as well as the influence of mechanical exfoliation and transferring process and the deformed flexible substrate.

Micro-Raman spectroscopy has been used as a noninvasive and versatile tool to map the mechanical strain/stress in large domain single crystalline materials on arbitrary substrates, such as MBE III–V materials, <sup>16</sup> graphene, <sup>17–19</sup> multilayered semiconductors, <sup>20</sup> metal oxides <sup>21</sup> and 2D layered chalcogenides. <sup>15</sup> As Raman peaks can be influenced by temperature, charge density, polarization, <sup>22,23</sup> and defects, it is critical to choose the phonon modes that are most sensitive to strain/stress. On the same sample, both the phonon frequency shift

Received: January 16, 2020 Accepted: March 19, 2020 Published: March 31, 2020





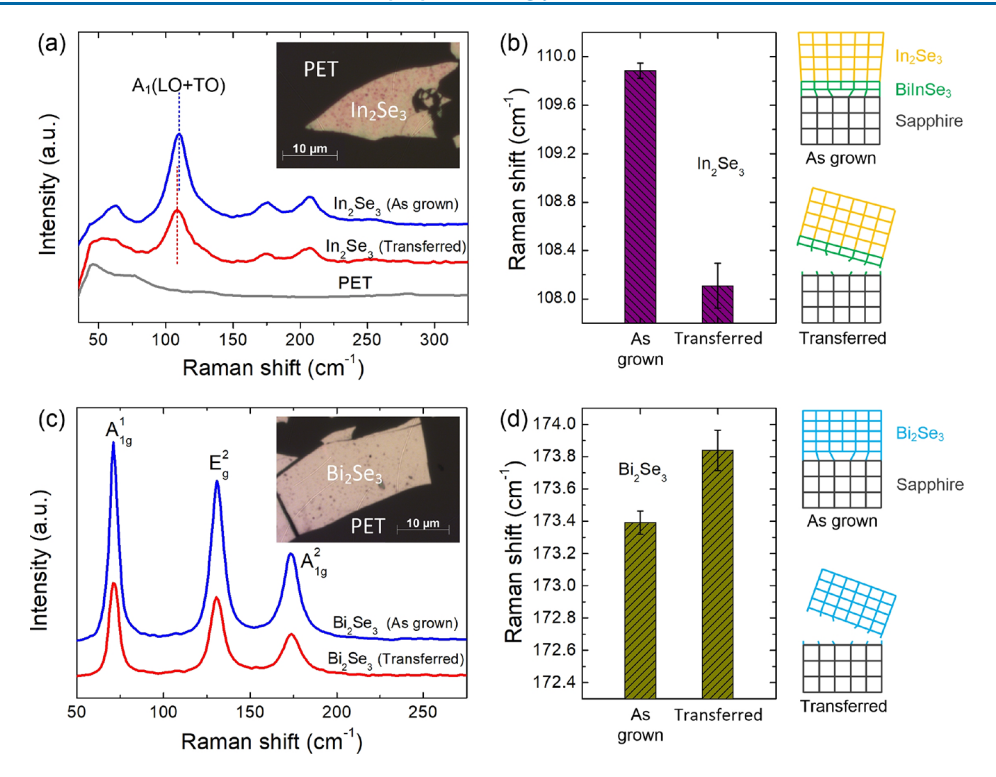


Figure 1. Micro-Raman shift of MBE-grown chalcogenide before and after transfer. (a) Micro-Raman spectra of MBE-grown  $In_2Se_3$  on a sapphire substrate (blue) and a mechanically exfoliated flake on an unknown flexible substrate (red curve), compared to the Raman response of substrate only (grey). Inset: Optical microscopy image of the exfoliated flake. (b) Peak wavenumber of the  $In_2Se_3$  Raman  $A_1$  (LO + TO) mode as marked in (a). Inset: Schematic of atomic structure transition before and after transferring. (c) Raman spectra of MBE  $Bi_2Se_3$  before (blue) and after (red) transferring. Inset: Optical microscopy image of the exfoliated flake. (d) Peak wavenumber of  $Bi_2Se_3$  Raman  $A_{1g}^2$  mode. Inset: Schematics of atomic structure transition before and after transferring. The peak wavenumbers are obtained by Lorentzian curve fitting of the experimental data.

and the full width at half maximum (FWHM) vary less than 0.1 cm $^{-1}$ . The charge density/doping level is uniform across the sample and remains unchanged before and after transferring, and thus the phonon frequency shift and FWHM broadening can be mostly attributed to strain/stress. In this work, we focus on the transverse optical vibrational  $A_1$  phonon mode. The  $In_2Se_3$   $A_1$  (LO + TO) mode and the  $Bi_2Se_3$   $A_{1g}^2$  mode are observed to be most sensitive to the externally applied strain. Linear potential deformation theory shows a linear relationship between the  $A_1$  phonon peak shift and strain (Supporting Information S1). The phonon frequency shift—strain coefficient can be experimentally calibrated and used to calculate the thickness-dependent strain in those samples through spatially resolved micro-Raman spectroscopy.

## 2. RESULTS AND DISCUSSION

**2.1. Strain in As-Grown and Transferred Chalcogenide Films.** Figure 1 compares the micro-Raman spectra of the as-grown and transferred MBE samples. The as-grown In<sub>2</sub>Se<sub>3</sub> sample (blue curve in Figure 1a) has three major peaks, which are representative phonon modes in  $\beta$ -In<sub>2</sub>Se<sub>3</sub>. A,6,7 The main peak around ~110 cm<sup>-1</sup> is attributed to the A<sub>1</sub>(LO + TO) mode. The other two peaks (175 and 205 cm<sup>-1</sup>) are relatively weak and attributed to the A<sub>1</sub>(TO) and A<sub>1</sub>(LO) modes, respectively. After transferring onto the polyethylene terephthalate (PET) substrate, no significant change in Raman spectra is observed (red curve in Figure 1a). An example of the transferred flake is shown as the inset in Figure 1a. The Raman peak from the PET substrate (grey curve in Figure 1a) is far from the major phonon frequency, and thus its influence can be excluded. Comparing the as-grown and transferred samples,

the major Raman  $A_1(TO + LO)$  mode shifts from 109.89 to  $108.11 \text{ cm}^{-1}$  (Figure 1b). Assuming the strain in the exfoliated samples is relaxed ( $\omega_{0\ln_2Se_3}=108.11 \text{ cm}^{-1}$ ), the phonon frequency shift ( $\sim 1.78 \text{ cm}^{-1}$ ) is caused by strain in the MBE growth. This zero-strain phonon frequency  $\omega_{0\ln_2Se_3}$  is consistent with the measured values reported by Zhou et al. <sup>24</sup> (108.5 cm<sup>-1</sup>) and Tang et al. <sup>25</sup> (108 cm<sup>-1</sup>) for the transferred  $\beta$ -In<sub>2</sub>Se<sub>3</sub> film. The BiInSe<sub>3</sub> buffer layer is less than 10 nm, and the In<sub>2</sub>Se<sub>3</sub> layer thickness is more than 70 nm. The Raman signal from the underlying buffer layer is an order of magnitude lower than the In<sub>2</sub>Se<sub>3</sub> signal. Also, BiInSe<sub>3</sub> has primary Raman peaks at 69.1, 129.1, and 171.7 cm<sup>-1</sup>, away from the In<sub>2</sub>Se<sub>3</sub>  $A_1(LO + TO)$  mode. <sup>26</sup>

Similar experiments are carried out for Bi<sub>2</sub>Se<sub>3</sub> (Figure 1c,d). MBE Bi<sub>2</sub>Se<sub>3</sub> shows three peaks centered at 71, 130, and 173 cm<sup>-1</sup>, corresponding to the  $A_{1g}^{1}$ ,  $E_{g}^{2}$ , and  $A_{1g}^{2}$  modes, respectively (Figure 1c).<sup>27</sup> After mechanical exfoliation and transferring, all three Raman modes shift to higher frequencies. The  $A_{1g}^{2}$  mode phonon frequency increases from 173.39 to 173.84 cm<sup>-1</sup> (Figure 1d). The measured phonon frequency shift with strain in the as-grown sample is -0.45 cm<sup>-1</sup>, and the measured zero-strain phonon frequency ( $\omega_{0Bi_2Se_3}$ ) is 173.84 cm<sup>-1</sup>. This value of the zero-strain phonon frequency is consistent with the value (174 cm<sup>-1</sup>) reported by Vilaplana et al.<sup>28</sup> and Dang et al.,<sup>29</sup> and close to the value (176.5 cm<sup>-1</sup>) reported by Chis et al.<sup>30</sup>

**2.2.** Calibration of Raman Shift—Strain Coefficient. To characterize the Raman shift—strain coefficient, we introduced controllable strain from bending the flexible substrate (Figure 2a) and simultaneously monitored the in situ Raman spectra of

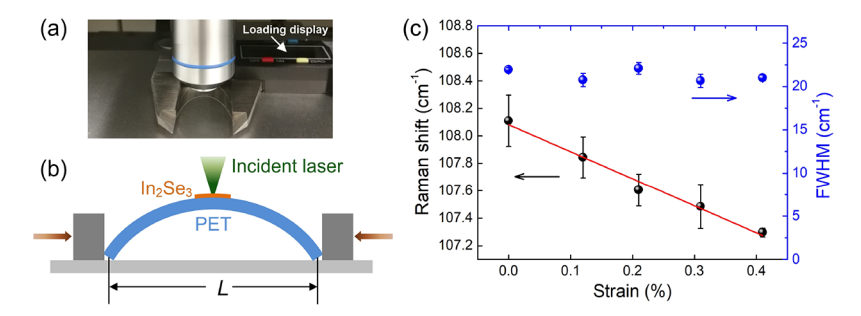


Figure 2. Strain-dependent Raman spectra of MBE  $In_2Se_3$ . (a) Optical image and (b) schematics of the strain-loading setup. The lateral length (L) is precisely measured using a caliper. (c) Raman peak wavenumber (black dots) and FWHM of  $A_1$  (LO + TO) vs the loaded strain. The linear curve fitting indicates that the Raman peak wavenumber shifts with effective strain applied onto the sample, at a ratio of -1.97 cm<sup>-1</sup>/% (red line).

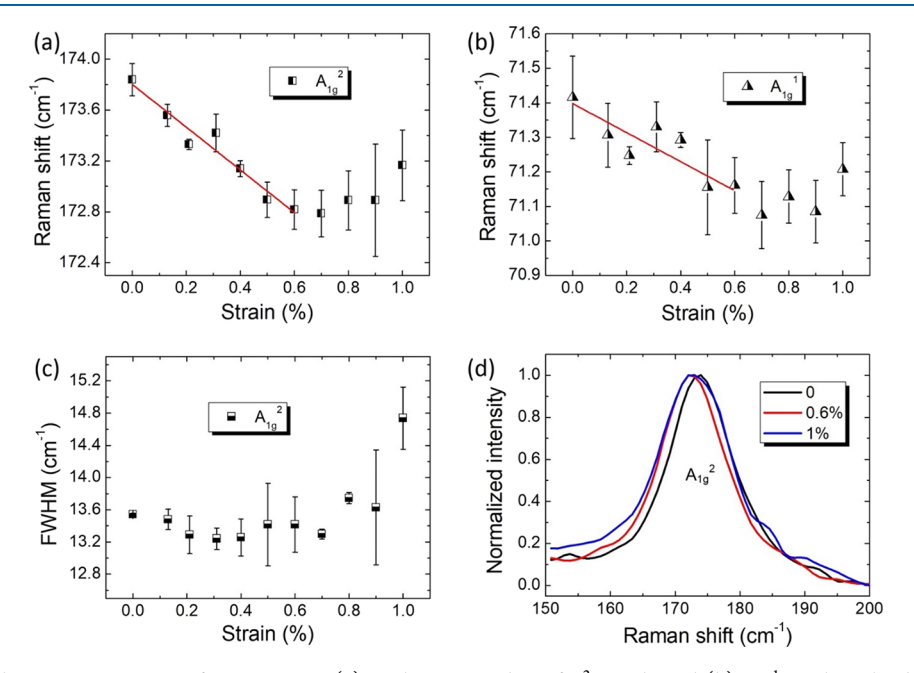


Figure 3. Strain-dependent Raman spectra of MBE  $Bi_2Se_3$ . (a) Peak wavenumber of  $A_{1g}^2$  mode and (b)  $A_{1g}^1$  mode vs loaded strain, at the ratio of -1.68 and -0.42 cm<sup>-1</sup>/% respectively. (c) FWHM of  $A_{1g}^2$  mode vs loaded strain. (d) Typical Raman spectra of  $A_{1g}^2$  mode under strain.

exfoliated samples in direct contact with the substrate. The samples are under uniaxial stress. The relationship between the Raman frequency shift of  $A_1$  mode  $\Delta\omega$  (= $\omega-\omega_0$ ) of point group  $D_3$  and the strain  $\varepsilon$  under uniaxial stress can be written as (Supporting Information S1)

$$\Delta \omega = \frac{(S_{11} + S_{12})a_{A_1} + S_{13}b_{A_1}}{S_{11}} \times \varepsilon = k\varepsilon$$
 (1)

where  $a_{A_1}$  and  $b_{A_1}$  are the strain phonon deformation potentials of  $A_1$  mode,  $S_{ij}$  is the material's compliance constant, and k is the Raman shift—strain coefficient of  $A_1$  mode under uniaxial stress. The strain introduced by curving the substrate is  $\varepsilon = \frac{t}{2R}$ . The flexible substrate thickness (t) is 0.175 mm. R is the radius of the curvature, and can be obtained through the following equation:  $\sin \frac{L_0}{2R} = \frac{L}{2R}$ , where  $L_0$  is the overall length of the PET and L is the lateral distance between the two edges (Figure 2b).

Figure 2c compares the  $In_2Se_3$  Raman spectra under different strain. The  $A_1(LO + TO)$  phonon frequency redshifts  $(\Delta\omega_{In_2Se_3} = \omega_{In_2Se_3} - \omega_{0In_2Se_3})$  with increasing strain  $(\varepsilon_{In_2Se_3})$  at the ratio of -1.97 cm<sup>-1</sup>/%. The ratio is obtained by linear

fitting the experimental data (black dots in Figure 2c). No significant increase of the FWHM is observed during the strain-loading process (blue dots in Figure 2c), which means that the load is effectively carried by the sample after stretching.

A similar method can calibrate the Raman shift–strain coefficient under uniaxial stress in the  $\rm Bi_2Se_3$  samples (Figure 3). The Raman peaks representing  $\rm A_{1g}^{\ 1},\,E_g^{\ 2},$  and  $\rm A_{1g}^{2}$  modes all red-shifted with the applied strain. The Raman shift–strain coefficient of  $\rm A_{1g}^{2}$  mode is calibrated to be  $-1.68~\rm cm^{-1}/\%$  (Figure 3a), compared to  $-0.42~\rm cm^{-1}/\%$  for the  $\rm A_{1g}^{\ 1}$  mode. Both parameters for the thin films are much larger than those reported for bulk structures.  $^{33}$ 

The FWHM of the Raman  $A_{1g}^2$  mode increases with applied strain as  $\varepsilon_{Bi_2Se_3} > 0.6\%$  (Figure 3c). As  $\varepsilon_{Bi_2Se_3}$  increases up to 1%, the Raman spectrum of  $A_{1g}^2$  mode partly overlaps with the one without any stress (Figure 3d). The increased FWHM indicates the nonuniform load carried with increasing strain. We attribute those observations to the failure of the weak vdW bonding at the interface. The interface failure leads to strain relaxation, and thus the phonon frequency recovers to its original position. This observation is consistent with other vdW contact interfaces reported in the literature. For example,

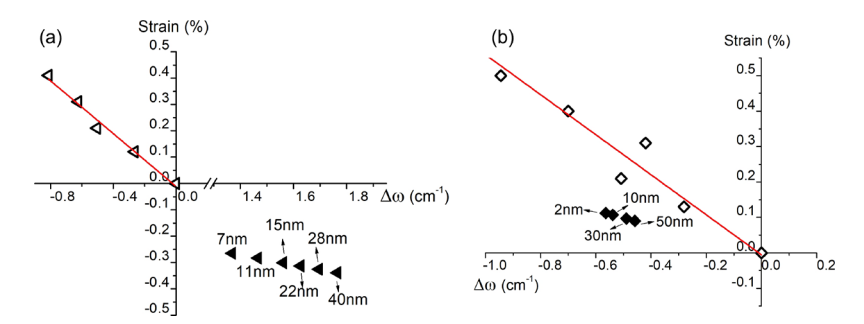


Figure 4. Strain vs phonon frequency shift for (a) In<sub>2</sub>Se<sub>3</sub> and (b) Bi<sub>2</sub>Se<sub>3</sub>. The linear fitting (red line) of the strain vs Raman frequency shift (empty marks), which is derived from Figures 2 and 3. The solid marks represent the estimated strain varying with film thickness.

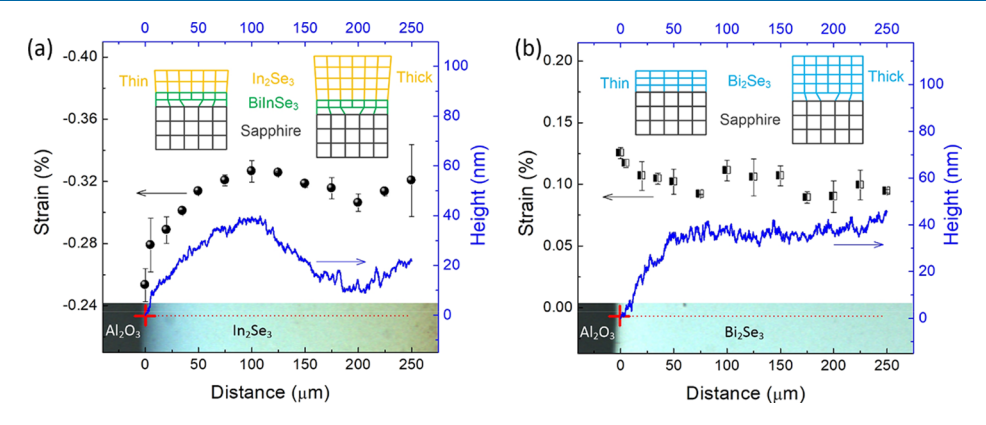


Figure 5. Thickness-dependent in-plane strain of (a) MBE  $In_2Se_3$  ( $A_1(LO + TO)$  mode) and (b)  $Bi_2Se_3$  ( $A_{1g}^2$  mode) on a sapphire substrate. Black dots: strain derived from the center wavenumber of Raman peaks. Blue curve: measured surface topology near the edge of the sample, as shown in the corresponding optical microscopy images. Insets: Schematics of atomic structure transition before and after transferring.

the interface between graphene and PET fails when the applied strain is above 0.5%. <sup>19</sup>

2.3. Thickness-Dependent Strain in As-Grown MBE Sample. Given the calibrated phonon frequency shift-strain coefficients, we can use spatially resolved micro-Raman spectroscopy to measure the strain introduced during the epitaxial growth process. Different from the uniaxial stress introduced by bending the substrate, the stress in the epitaxial layer is biaxial. The relationship between the phonon frequency shift and the strain under biaxial stress is also linear. For Bi<sub>2</sub>Se<sub>3</sub>, the Raman shift-strain coefficient under uniaxial stress is derived from being 0.37 times of the one under biaxial stress (Supporting Information S1). Because of the limited literature report, the relationship between the two coefficients cannot be accurately estimated for In<sub>2</sub>Se<sub>3</sub>. Given the similar crystalline structure, we assume the ratio between two coefficients in In<sub>2</sub>Se<sub>3</sub>. From the experimentally measured Raman shift, we can estimate the local in-plane strain formed during the material growth process. The sample thickness increases from zero to tens of nanometers near the edge of the MBE sample, and thus the spatially resolved Raman spectra can be used to calculate the strain in the sample as a function of thickness. Figure 4 plots strain versus phonon frequency shifts in In<sub>2</sub>Se<sub>3</sub> and Bi<sub>2</sub>Se<sub>3</sub>. The empty triangular marks in Figure 4a are experimentally measured data through substrateloaded strain in In<sub>2</sub>Se<sub>3</sub> on PET substrates. By extrapolating the linear curve fitted line (red line in Figure 4a), the strain in the MBE-grown sample with increasing thickness can be estimated through its phonon frequency (solid triangular marks in Figure 4a). The same process/analysis is applied to Bi<sub>2</sub>Se<sub>3</sub> samples (Figure 4b). The results indicate that compression strain exists

in the  $\rm In_2Se_3$  sample and increases with the sample thickness. In a 40 nm thick film, the compression strain reaches -0.33%.  $\beta\text{-In}_2Se_3$  can load large compression strain,<sup>34</sup> and thus the Raman shift—strain relationship is likely to be valid in the region  $0 > \varepsilon_{\rm In}_2Se_3 > -0.5\%$ . Distinguished from  $\rm In}_2Se_3$ , the tensile strain is observed in  $\rm Bi}_2Se_3$ , and the strain decreases with film thickness (solid black marks in Figure 4b). The observation is consistent with the literature. <sup>15</sup>

The strain mapping is carried out near the edge of the MBE sample, where the film thickness is not uniform (Figure 5). The spatially resolved strain (derived from Figure 4) is compared to the film thickness. A similar trend between the compression strain and the film thickness is observed in the In<sub>2</sub>Se<sub>3</sub> sample (Figure 5a), while the tensile strain is inversely related to the film thickness in the Bi<sub>2</sub>Se<sub>3</sub> sample (Figure 5b). It is observed that the phonon frequency variation is much more sensitive to the film thickness in In<sub>2</sub>Se<sub>3</sub> than Bi<sub>2</sub>Se<sub>3</sub>.

The opposite strain—thickness relationship in  $\beta$ -In<sub>2</sub>Se<sub>3</sub> and Bi<sub>2</sub>Se<sub>3</sub> can be explained by the different atomic deformation on the heteroepitaxy interfaces. The tensile strain in Bi<sub>2</sub>Se<sub>3</sub> is more straightforward to explain. Its lattice constant in the a—b plane is 0.414 nm,<sup>35</sup> which is smaller than the sapphire substrate (0.476 nm for the plane a—b). During the deposition of the first few layers, tensile strain is formed on the interface (Figure 5b). With increasing thickness, the strain becomes larger, and dislocations may be formed. These dislocations will be formed near the interface, and thus the strain is relaxed in thicker films. Alternatively, the strain could be relaxed through slight changes in the lattice constant with thickness because of the weak vdW bonds between layers. Either way, we expect the smaller strain that is observed in thicker samples. In addition,

the thermal expansion coefficient of  $Bi_2Se_3$  (11 × 10<sup>-6</sup>/°C<sup>36</sup>) is larger than that of sapphire (7.5 × 10<sup>-6</sup>/°C). The cooling process in the growth chamber will also therefore contribute to the development of tensile strain.

The most likely cause of the strain in the In<sub>2</sub>Se<sub>3</sub> layer is the difference in thermal expansion between the seed layer and the In<sub>2</sub>Se<sub>3</sub> film. We can see from the data shown in Figure 5a that the 10 nm seed layer accommodates most of the strain caused by the difference in the lattice constant between the chalcogenide film and the sapphire substrate. The compressive strain in the In<sub>2</sub>Se<sub>3</sub> film can be attributed to a significant difference in the thermal expansion coefficient between the film and the seed layer and the substrate: the thermal expansion coefficient of  $In_2Se_3$  is  $3 \times 10^{-6}$ /°C, 37 while the thermal expansion coefficient of the seed layer is likely to be between the In<sub>2</sub>Se<sub>3</sub> and Bi<sub>2</sub>Se<sub>3</sub> values at  $11 \times 10^{-6}$ /°C. The thermal expansion coefficient of sapphire is  $7.5 \times 10^{-6}$ /°C. Therefore, as the sample cools from its growth temperature of 425 °C, the compressive strain will be induced in the film. Assuming the lattice deformation in In<sub>2</sub>Se<sub>3</sub> is minimal at the growth temperature, the larger thermal expansion coefficient in the seed layer and the substrate makes its lattice experience a larger reduction compared to In2Se3, which leads to compressive strain in the epitaxial layer. This also explains why we see an increase in the strain as the film thickness increases for In<sub>2</sub>Se<sub>3</sub>.

## 3. CONCLUSIONS

We report the micro-Raman study of the strain in MBE-grown chalcogenide samples. The A<sub>1</sub>(LO + TO) peak in In<sub>2</sub>Se<sub>3</sub> and the A<sub>1g</sub><sup>2</sup> peak in Bi<sub>2</sub>Se<sub>3</sub> are the phonon modes most sensitive to externally introduced strain, and thus used to calibrate the strain in as-grown samples. The In<sub>2</sub>Se<sub>3</sub> A<sub>1</sub>(LO + TO) phonon frequency decreases with strain at the ratio of  $-1.97 \text{ cm}^{-1}/\%$ . The Raman shift-strain coefficient for the A<sub>1g</sub> mode in Bi<sub>2</sub>Se<sub>3</sub> is calibrated to be  $-1.68 \text{ cm}^{-1}/\%$ , by introducing strain in a flexible substrate. Micro-Raman studies indicate that the strain increases with the thickness in In<sub>2</sub>Se<sub>3</sub> and decreases in Bi<sub>2</sub>Se<sub>3</sub>, which might be attributed to the opposite differences in both the lattice constant and the thermal expansion coefficient between the sample and the substrate. Understating the strain sheds light on the possible atomic structure deformations in the MBE chalcogenide films, and the modified band diagrams can be used for evaluating their performance in optoelectronic devices.

# 4. METHODS

**4.1. Material Growth.** All chalcogenide thin films are grown on c-plane sapphire substrates. In the MBE chamber (Veeco GENxplor), selenium is evaporated by using a cracker source, and indium and bismuth are both evaporated using dual filament effusion cells. A thermocouple monitors the substrate temperature. Before growth, the sapphire substrate is heated to 650 °C for cleaning, and then reduced to 300 °C for the growth of Bi<sub>2</sub>Se<sub>3</sub>. Bi<sub>2</sub>Se<sub>3</sub> is then directly grown on the sapphire substrate. Unfortunately, it is difficult to nucleate a single polytype of In<sub>2</sub>Se<sub>3</sub> on sapphire. Therefore, a seed layer of 10 QL BiInSe<sub>3</sub> is needed for the growth of In<sub>2</sub>Se<sub>3</sub>. To grow the seed layer, 5 QL Bi<sub>2</sub>Se<sub>3</sub> and 5 QL In<sub>2</sub>Se<sub>3</sub> are first grown on the sapphire substrate at 300 °C. Then, the sample is heated to 425 °C for interlayer diffusion. After the BiInSe<sub>3</sub> seed layer (10 nm thick) is grown, pure In<sub>2</sub>Se<sub>3</sub> layers are deposited at 425 °C.

Atomic force microscopy measurements confirm the formation of large domains of single crystalline  $Bi_2Se_3$  and  $In_2Se_3$ . The thickness of MBE  $Bi_2Se_3$  and  $In_2Se_3$  films is characterized to be 79 and 76 nm respectively, using a Bruker DektakXT profilometer.

- **4.2. Mechanical Exfoliation and Transfer.** Large flakes of MBE-grown In<sub>2</sub>Se<sub>3</sub> and Bi<sub>2</sub>Se<sub>3</sub> thin films can be exfoliated from the sapphire substrate and transferred onto a 0.175 mm thick PET using a thermal release tape (Supporting Information S2). The MBE flakes are relieved from the thermal release tape after heating up to 110 °C.
- **4.3. Characterization.** The chalcogenide crystalline film on a flexible substrate is then mounted on a caliber and placed under a micro-Raman spectrometer with a  $50\times$  objective and a 900 lines/mm grating. The strain is applied to the sample by reducing the lateral distance of the bent PET. The micro-Raman spectrometer (Thermo Scientific DXR) uses a 532 nm excitation laser, with the laser power kept below 0.1 mW for minimizing the possible thermal effect on the sample. The spot size is around 0.7  $\mu$ m. It is noted that sometimes the strain from the substrate may not be able to directly load onto the wrinkled sample before expanding the folded area. Those wrinkles are likely introduced during the dry transfer process.

## ASSOCIATED CONTENT

## Supporting Information

The Supporting Information is available free of charge at https://pubs.acs.org/doi/10.1021/acsomega.0c00224.

Derivation of Raman shift-strain relationships and details of chalcogenide material exfoliation and transfer (PDF)

## AUTHOR INFORMATION

## **Corresponding Authors**

Qiu Li — Tianjin Key Laboratory of High Speed Cutting and Precision Machining, Tianjin University of Technology and Education, Tianjin 300222, China; Department of Electrical and Computer Engineering, University of Delaware, Newark, Delaware 19716, United States; orcid.org/0000-0001-5288-0095; Email: liqiu@tute.edu.cn

Tingyi Gu — Department of Electrical and Computer Engineering, University of Delaware, Newark, Delaware 19716, United States; ⊚ orcid.org/0000-0003-0414-6333; Email: tingyigu@udel.edu

## **Authors**

Yong Wang — Department of Materials Science and Engineering, University of Delaware, Newark, Delaware 19716, United States

**Tiantian Li** — Department of Electrical and Computer Engineering, University of Delaware, Newark, Delaware 19716, United States

Wei Li – Department of Materials Science and Engineering, University of Delaware, Newark, Delaware 19716, United States

Feifan Wang — Department of Electrical and Computer Engineering, University of Delaware, Newark, Delaware 19716, United States; State Key Laboratory for Mesoscopic Physics & Department of Physics Collaborative Innovation Center of Quantum Matter, Peking University, Beijing 100871, China Anderson Janotti — Department of Materials Science and Engineering, University of Delaware, Newark, Delaware 19716, United States

Stephanie Law — Department of Materials Science and Engineering, University of Delaware, Newark, Delaware 19716, United States; orcid.org/0000-0002-5087-6663

Complete contact information is available at: https://pubs.acs.org/10.1021/acsomega.0c00224

#### Notes

The authors declare no competing financial interest.

# ACKNOWLEDGMENTS

Q.L. acknowledges support from the National Natural Science Foundation of China (nos. 11772227 and 11772223) and the Innovation Team Training Plan of Tianjin Universities and Colleges (no. TD13-5096). This work was financially supported by Air Force Office of Scientific Research (AFOSR YIP FA9550-18-1-0300) and National Aeronautics and Space Administration (NASA ECF 80NSSC17K0526). Y.W. and S.L. acknowledge support from the U.S. Department of Energy, Office of Science, Office of Basic Energy Sciences (DE-SC0016380). T.L. acknowledges partial support from the Open Foundation of State Kay Laboratory of Advanced Optical Communication Systems and Networks, China. W.L. and A.J. acknowledge support from the NSF Faculty Early Career Development Program DMR-1652994.

## REFERENCES

- (1) Hsieh, D.; Xia, Y.; Qian, D.; Wray, L.; Dil, J. H.; Meier, F.; Osterwalder, J.; Patthey, L.; Checkelsky, J. G.; Ong, N. P.; Fedorov, A. V.; Lin, H.; Bansil, A.; Grauer, D.; Hor, Y. S.; Cava, R. J.; Hasan, M. Z. A tunable topological insulator in the spin helical Dirac transport regime. *Nature* **2009**, *460*, 1101–1105.
- (2) Hasan, M. Z.; Kane, C. L. Colloquium: Topological Insulators. *Rev. Mod. Phys.* **2010**, 82, 3045–3067.
- (3) Ye, J.; Soeda, S.; Nakamura, Y.; Nittono, O. Crystal structures and phase transformation in  $In_2Se_3$  compound semiconductor. *Jpn. J. Appl. Phys.* **1998**, 37, 4264–4271.
- (4) Balakrishnan, N.; Staddon, C. R.; Smith, E. F.; Stec, J.; Gay, D.; Mudd, G. W.; Makarovsky, O.; Kudrynskyi, Z. R.; Kovalyuk, Z. D.; Eaves, L.; Patanè, A.; Beton, P. H. Quantum confinement and photoresponsivity of  $\beta$ -In<sub>2</sub>Se<sub>3</sub> nanosheets grown by physical vapour transport. 2D Mater **2016**, 3, 025030.
- (5) Wang, Y.; Ginley, T. P.; Law, S. Growth of high-quality Bi<sub>2</sub>Se<sub>3</sub> topological insulators using (Bi1-xInx)<sub>2</sub>Se<sub>3</sub> buffer layers. J. Vac. Sci. Technol., B: Nanotechnol. Microelectron.: Mater., Process., Meas., Phenom. 2018, 36, 02D101.
- (6) Rasmussen, A. M.; Teklemichael, S. T.; Mafi, E.; Gu, Y.; McCluskey, M. D. Pressure-induced phase transformation of In<sub>2</sub>Se<sub>3</sub>. *Appl. Phys. Lett.* **2013**, *102*, 062105.
- (7) Tao, X.; Gu, Y. Crystalline—crystalline phase transformation in two-dimensional  $\rm In_2Se_3$  thin layers. *Nano Lett.* **2013**, *13*, 3501–3505.
- (8) Li, W.; Sabino, F. P.; De Lima, F. C.; Wang, T.; Miwa, R. H.; Janotti, A. Large disparity between optical and fundamental band gaps in layered In<sub>2</sub>Se<sub>3</sub>. *Phys. Rev. B* **2018**, *98*, 165134.
- (9) Luo, S.; He, L.; Li, M. Chiral interaction between spin-momentum locked photons and surface electrons in topological insulators. *Nat. Commun.* **2017**, *8*, 2141.
- (10) McIver, J. W.; Hsieh, D.; Steinberg, H.; Jarillo-Herrero, P.; Gedik, N. Control over topological insulator photocurrents with light polarization. *Nat. Nanotechnol.* **2012**, *7*, 96–100.
- (11) Zhang, H.; Zhang, X.; Liu, C.; Lee, S.-T.; Jie, J. High-responsivity, high-detectivity, ultrafast topological insulator Bi<sub>2</sub>Se<sub>3</sub>/silicon heterostructure broadband photodetectors. *ACS Nano* **2016**, *10*, 5113–5122.

- (12) Sze, S. M.; Ng, K. K. Physics of Semiconductor Devices; John Wiley & Sons: New York, 2006.
- (13) Park, J. Y.; Lee, G.-H.; Jo, J.; Cheng, A. K.; Yoon, H.; Watanabe, K.; Taniguchi, T.; Kim, M.; Kim, P.; Yi, G.-C. Molecular beam epitaxial growth and electronic transport properties of high quality topological insulator Bi2Se3 thin films on hexagonal boron nitride. 2D Mater. 2016, 3, 035029.
- (14) Wang, Y.; Law, S. Optical properties of (Bi1-xInx)<sub>2</sub>Se<sub>3</sub> thin films. Opt. Mater. Express **2018**, 8, 2570–2578.
- (15) Li, B.; Chen, W.; Guo, X.; Ho, W.; Dai, X.; Jia, J.; Xie, M. Strain in epitaxial high-index Bi<sub>2</sub>Se<sub>3</sub> (221) films grown by molecular-beam epitaxy. *Appl. Surf. Sci.* **2017**, *396*, 1825–1830.
- (16) Tripathy, S.; Chua, S. J.; Chen, P.; Miao, Z. L. Micro-Raman investigation of strain in GaN and AlxGa1-xN/GaN heterostructures grown on Si(111). *J. Appl. Phys.* **2002**, *92*, 3503–3510.
- (17) Ferrari, A. C.; Basko, D. M. Raman spectroscopy as a versatile tool for studying the properties of graphene. *Nat. Nanotechnol.* **2013**, *8*, 235–246.
- (18) Lee, J. E.; Ahn, G.; Shim, J.; Lee, Y. S.; Ryu, S. Optical separation of mechanical strain from charge doping in graphene. *Nat. Commun.* **2012**, *3*, 1024.
- (19) Xu, C.; Xue, T.; Qiu, W.; Kang, Y. Size Effect of the Interfacial Mechanical Behavior of Graphene on a Stretchable Substrate. ACS Appl. Mater. Interfaces 2016, 8, 27099–27106.
- (20) Qiu, W.; Cheng, C.-L.; Liang, R.-R.; Zhao, C.-W.; Lei, Z.-K.; Zhao, Y.-C.; Ma, L.-L.; Xu, J.; Fang, H.-J.; Kang, Y.-L. Measurement of residual stress in a multi-layer semiconductor heterostructure by micro-Raman spectroscopy. *Acta Mech. Sin.* **2016**, 32, 805–812.
- (21) Li, Q.; Gou, Y.; Wang, T.-G.; Gu, T.; Yu, Q.; Wang, L. Study on local residual stress in the nanocrystalline Cr<sub>2</sub>O<sub>3</sub> coating by micro-Raman spectroscopy. *Coatings* **2019**, *9*, 500.
- (22) Ma, L.; Fan, X.; Qiu, W. Polarized Raman spectroscopy-stress relationship considering shear stress effect. *Opt. Lett.* **2019**, *44*, 4682–4685
- (23) Volodin, V. A.; Sinyukov, M. P.; Sachkov, V. A.; Stoffel, M.; Rinnert, H.; Vergnat, M. Optical phonons as a probe to determine both composition and strain in  $In_xAl_{(1-x)}$  As quantum dots embedded in an AlAs matrix. *Europhys. Lett.* **2014**, *105*, 16003.
- (24) Zhou, S.; Tao, X.; Gu, Y.; Gu, Y. Thickness-dependent thermal conductivity of suspended two-dimensional single-crystal In<sub>2</sub>Se<sub>3</sub> layers grown by chemical vapor deposition. *J. Phys. Chem. C* **2016**, *120*, 4753–4758.
- (25) Tang, L.; Teng, C.; Luo, Y.; Khan, U.; Pan, H.; Cai, Z.; Zhao, Y.; Liu, B.; Cheng, H. M. Confined van der Waals epitaxial growth of two-dimensional large single-crystal In<sub>2</sub>Se<sub>3</sub> for flexible broadband photodetectors. *Research* **2019**, *2019*, 2763704.
- (26) Yao, J. D.; Zheng, Z. Q.; Yang, G. W. Alloying-assisted phonon engineering of layered BiInSe<sub>3</sub>@nickel foam for efficient solar-enabled water evaporation. *Nanoscale* **2017**, *9*, 16396–16403.
- (27) Yan, Y.; Zhou, X.; Jin, H.; Li, C.-Z.; Ke, X.; Van Tendeloo, G.; Liu, K.; Yu, D.; Dressel, M.; Liao, Z.-M. Surface-facet-dependent phonon deformation potential in individual strained topological insulator Bi<sub>2</sub>Se<sub>3</sub> nanoribbons. *ACS Nano* **2015**, *9*, 10244–10251.
- (28) Vilaplana, R.; Santamaria-Perez, D.; Gomis, O.; Manjon, F. J.; Gonzalez, J.; Segura, A.; Munoz, A.; Rodriguez, P.; Pérez-González, E.; Marin-Borras, V.; Muñoz-Sanjoséet, V.; Drasar, C.; Kucek, V. Structural and vibrational study of Bi<sub>2</sub>Se<sub>3</sub> under high pressure. *Phys. Rev. B: Condens. Matter Mater. Phys.* **2011**, *84*, 184110.
- (29) Dang, W.; Peng, H.; Li, H.; Wang, P.; Liu, Z. Epitaxial heterostructures of ultrathin topological insulator nanoplate and graphene. *Nano Lett.* **2010**, *10*, 2870–2876.
- (30) Chis, V.; Sklyadneva, I. Y.; Kokh, K. A.; Volodin, V. A.; Tereshchenko, O. E.; Chulkov, E. V. Vibrations in binary and ternary topological insulators: first-principles calculations and Raman spectroscopy measurements. *Phys. Rev. B: Condens. Matter Mater. Phys.* **2012**, *86*, 174304.
- (31) Suo, Z.; Ma, E. Y.; Gleskova, H.; Wagner, S. Mechanics of rollable and foldable film-on-foil electronics. *Appl. Phys. Lett.* **1999**, 74, 1177–1179.

- (32) Lee, J.; Ha, T.-J.; Li, H.; Parrish, K. N.; Holt, M.; Dodabalapur, A.; Ruoff, R. S.; Akinwande, D. 25 GHz embedded-gate graphene transistors with high-k dielectrics on extremely flexible plastic sheets. *ACS Nano* **2013**, *7*, 7744–7750.
- (33) Vilaplana, R.; Santamaría-Pérez, D.; Gomis, O.; Manjón, F.; González, J.; Segura, A.; Munoz, A.; Rodríguez-Hernández, P.; Pérez-González, E.; Marín-Borrás, V. Structural and Vibrational Study of Bi<sub>2</sub>Se<sub>3</sub> under High Pressure. *Phys. Rev. B: Condens. Matter Mater. Phys.* **2011**, *84*, 184110.
- (34) Vilaplana, R.; Parra, S. G.; Jorge-Montero, A.; Rodríguez-Hernández, P.; Munoz, A.; Errandonea, D.; Segura, A.; Manjón, F. J. Experimental and theoretical studies on  $\alpha$ -In<sub>2</sub>Se<sub>3</sub> at high pressure. *Inorg. Chem.* **2018**, *57*, 8241–8252.
- (3Š) Qiu, X.-f.; Zhu, J.-J.; Pu, L.; Shi, Y.; Zheng, Y.-D.; Chen, H.-Y. Size-controllable sonochemical synthesis of thermoelectric material of Bi<sub>2</sub>Se<sub>3</sub> nanocrystals. *Inorg. Chem. Commun.* **2004**, *7*, 319–321.
- (36) Chen, X.; Zhou, H. D.; Kiswandhi, A.; Miotkowski, I.; Chen, Y. P.; Sharma, P. A.; Lima Sharma, A. L.; Hekmaty, M. A.; Smirnov, D.; Jiang, Z. Thermal expansion coefficients of Bi<sub>2</sub>Se<sub>3</sub> and Sb<sub>2</sub>Te<sub>3</sub> crystals from 10 K to 270 K. *Appl. Phys. Lett.* **2011**, *99*, 261912.
- (37) Popovic, S.; Tonejc, A.; Grzeta-Plenkovic, B.; Celustka, B.; Trojko, R. Revised and new crystal data for indium selenides. *Appl. Crystallogr.* **1979**, *12*, 416–420.